metals

Article

Characteristic Flow Behavior and Processing Map of a Novel Lean Si Spring Steel for Automotive Stabilizer Bars

Hongbo Pan [1,2], Shiwei Li [1,2], Jing Ding [3,4], Weiming Liu [1,2], Yanan Fu [1,2], Xiaohui Shen [3,*], Hailian Wei [5,6,*], Huiting Wang [3], Liang Yu [4] and Qiang Fang [4]

1 Key Laboratory of Metallurgical Emission Reduction & Resources Recycling of Ministry of Education, Anhui University of Technology, Ma'anshan 243002, China
2 Anhui Province Key Laboratory of Metallurgical Engineering & Resource Recycling, Anhui University of Technology, Ma'anshan 243002, China
3 School of Metallurgical Engineering, Anhui University of Technology, Ma'anshan 243002, China
4 Special Steel Branch, Ma'anshan Iron and Steel Co., Ltd., Ma'anshan 243000, China
5 School of Materials Science and Engineering, Anhui University of Technology, Ma'anshan 243002, China
6 Key Laboratory of Green Fabrication and Surface Technology of Advanced Metal Materials, Ministry of Education, Anhui University of Technology, Ma'anshan 243002, China
* Correspondence: sxh_ahut@163.com (X.S.); whl1988@ahut.edu.cn (H.W.)

Abstract: The spring steel for automotive stabilizer bars has a great responsibility in that its quality directly affects the stability, safety, and comfort of vehicle operation. The isothermal thermal compression behavior of a novel lean Si spring steel that was used to manufacture an anti-roll bar was investigated with a DIL805A/D quenching thermal dilatometer in this research. A hyperbolic sine type of constitutive model was established, and hot processing maps were produced to evaluate the experimental steel's hot workability properties. The experimental results suggest that dynamic recrystallization (DRX) preferentially occurs at a low strain rate and high thermal processing temperature, while the processing maps of the experimental steel are susceptible to strain. The instability regions increase as the strain increases. The processing maps' stable and instable domains should be decided upon comprehensive analysis of the instability criterion, power dissipation efficiency, and strain rate sensitivity index. The optimum parameters of hot processing for the experimental steel at various strains are that the deformation temperature of 1000–1150 °C and the strain rate of 0.1, approximately.

Keywords: 55Cr3 spring steel; hot compression; flow characteristic; constitutive model; processing maps

Citation: Pan, H.; Li, S.; Ding, J.; Liu, W.; Fu, Y.; Shen, X.; Wei, H.; Wang, H.; Yu, L.; Fang, Q. Characteristic Flow Behavior and Processing Map of a Novel Lean Si Spring Steel for Automotive Stabilizer Bars. *Metals* **2023**, *13*, 44. https://doi.org/10.3390/met13010044

Academic Editor: Hana Jirková

Received: 29 November 2022
Revised: 18 December 2022
Accepted: 22 December 2022
Published: 24 December 2022

1. Introduction

As an important element of the manufacturing industry, spring steel is widely used in automobiles, railways, electrical appliances, and other fields. Among them, the automotive industry has a great demand for spring steel, accounting for 60% of the total consumption of spring steel [1]. The stabilizer bar is a major applications of spring steel in automobiles [2], being horizontally installed in the automobile suspension system to improve the vehicle's stability [3–6], that is, the anti-roll bar (ARB) prevents lateral roll caused by bumpy roads, load, and excessive speed during maneuvering [7,8]. Vehicle rollover is a severe social issue that results in loss of life as well as environmental and financial effects [9–11]. The ARB plays a decisive role in ensuring the safety of automobiles. Fatigue failure of anti-roll bar will occur during the vehicle operation, owing to cyclic bending, torsion, and other alternating stresses [12–14]. In general, the most efficient method to extend fatigue life is to reduce stress localization at a crucial mechanical component position. Therefore, materials and components are required to have a fine and homogeneous microstructure and high surface quality.

Currently, the anti-roll bar is generally manufactured with 55Cr3 spring steel by hot rolling, cold sawing, straightening, hot forging, hot bending, trimming, punching, quenching, tempering, and surface strengthening, having a U-shaped profile [15,16]. In these processes, hot rolling and hot forging directly affect the homogenization and refinement of the microstructure and surface quality of finished products [17,18]. Therefore, investigating the effect of high-temperature deformation on microstructural refinement is critical for improving final mechanical properties [19–21]. By regulating dynamic recrystallization and dynamic recovery, the high-temperature deformation process can effectively refine the prior austenite grains, consequently refining the martensite structure and enhancing the final mechanical properties [22–25]. In addition, medium- and small-sized wires or bars would preferably be transformed into martensite during hot rolling due to the excellent hardenability of 55Cr3 spring steel, which makes it difficult for downstream anti-roll bar manufacturers to cut. Thus, anti-roll bar manufacturers have a preference for raw materials with relatively low hardness provided by the steel manufacturing industry to facilitate cutting. Therefore, low-temperature rolling deformation is conducted by the steel manufacturing industry to obtain wires and bars with low hardness through deformation-induced phase transformation. However, inappropriate temperature and reduction during low-temperature deformation will cause microcracks on the surface of materials or parts, resulting in stress localization during application and reducing service life. Over the last few years, the processing maps premised on the dynamic materials model (DMM) are widely applied to significantly improve thermal processing technology [26]. In light of a processing map, an appropriate processing parameter can not only be obtained, but also instable flow of metals could be avoided, thus contributing to the optimized hot rolling or hot forging technology [27].

The hot compression characteristics of materials can be effectively used to establish relationships between various deformation situations and the evolution of microstructure [28]. The complicated deformation mechanisms containing work hardening, dynamic recovery [29], dynamic recrystallisation [30], and flow instability [31] normally occur during hot compression. Therefore, the correlations among hot deformation process parameters, the constitutive relation, and flow instability are the principal investigation spotlights for insights into material flow behavior. In the past decades, the constitutive models and processing map of various micro-alloy and high-alloy steels have been preciously determined to predict their high-temperature flow behaviors [32]. However, limited literature [33–35] has reported the flow behavior of spring steel. Moreover, the relevant research of a lean Si spring steel dominated by Cr has yet to be discovered.

This research focuses on investigating the flow behavior of a lean Si spring steel dominated by Cr and establishing the constitutive modeling and the processing map during the compression process at elevated temperature. The experimental scheme designed in this research is based on the conditions of commercial anti-roll bar hot rolling and hot forging. As a result, this work is extremely valuable to the industry, and the results may be effectively applied in steel and anti-roll bar practical production. The constructed model and processing map based upon hot deformation experiment data can provide a reference for the practical anti-roll bar hot deformation process.

2. Experimental Procedure

The experimental materials were obtained from commercial continuous casting square billet manufactured with a 100t electric furnace; the main alloy element content of the tested 55Cr3 steel is summarized in Table 1, with it being a lean Si spring steel with a predominance of Cr.

Table 1. The main alloy element content of the tested 55Cr3 steel (wt %).

C	Si	Mn	P	S	Cr	Ni	Mo	V
0.52~0.59	≤0.40	0.70~1.00	≤0.015	≤0.015	0.70~1.00	≤0.20	≤0.10	≤0.10

To investigate the flow characteristics of the tested materials, thermal compression simulations were conducted on DIL805A/D quenching thermal dilatometer with a vacuum degree of 1×10^{-5}, during which, flow characteristic curves were recorded automatically. Experimental cylindrical specimens were extracted from a continuous square billet with diameter of 5 mm and height of 10 mm. To investigate the behaviors of dynamic softening, the thermal processing temperatures ranging from 850 to 1150 °C and the strain rates ranging from 0.01 to 10 s^{-1} were selected as the tested conditions. Figure 1 illustrates the deformation process and specific process parameters schematically. To make austenite microstructure homogeneously distribute, all the samples were first heated until 1230 °C with a rate of 10 °C/s, and subsequently were soaked for 300 s and then deformed. Before deformation, the specimens were firstly cooled to deformation conditions at a rate of 5 °C/s and then held for 20 seconds to obtain uniform deformation temperatures. After that, the samples were deformed at a total reduction ratio of 60% (equivalent to the true strain of 0.9) and then rapidly quenched with water until ambient temperature.

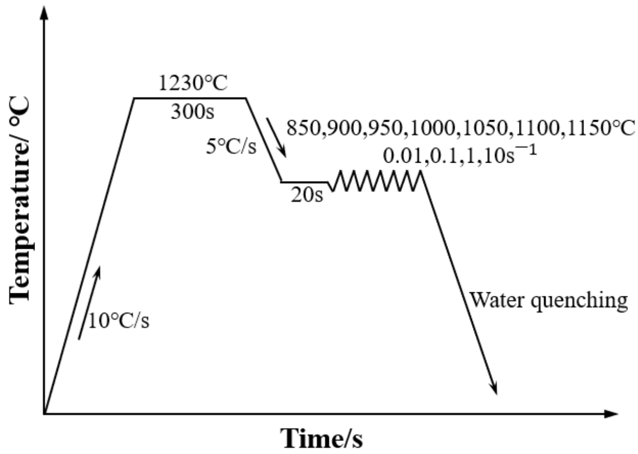

Figure 1. Schematic process for hot compression.

3. Results and Discussion

3.1. Flow Characteristics

In view of the test results, the representative flow behaviors of the tested steel following thermal compression at given experimental conditions are depicted in Figure 2. An evident finding is that the true stress was sensitive to various deformation conditions. The variation in flow curves ascribes to strain hardening and dynamic softening during the elevated temperature compression [36]. Figure 2 clearly shows that the flow stress had a positive correlation with the strain rate and a negative correlation with the deformation temperature. Moreover, the typical DRX flow behavior with a single peak feature was more likely to occur at a high thermal processing temperature and low strain rate, as displayed in Figure 2a,b. The occurrence of the flow curve peak was ascribed to a dynamic balance between the strain hardening and the dynamic softening due to DRX and DRV with the strain increases [37]. Moreover, it was found that both the peak stress and corresponding strain level deceased gradually as the thermal processing temperature rose and the strain rate declined, as illustrated in Figure 3. Conversely, the work hardening flow characteristics were more obvious at the low thermal compression temperature and the high strain rate, as revealed in Figure 2c,d. In addition, Figure 2d presents the appearance of a serrated flow curve at a relatively low thermal compression temperature and high strain rate that represents typical dynamic strain aging feature [38,39]. In principle, hot compression is a non-isothermal process since microstructure evolution and temperature rise would endure the consumption of partial instantaneous power during the thermal–mechanical process [40]. It is more evident that thermal softening would result in a decrease in flow stress that is attributable to temperature rise at lower deformation temperatures and higher strain rates, while large strain results in work hardening [41,42]. The interaction of temperature rise softening and work hardening results in serrated flow curve [43]. Thus, the whole thermal compression process of the tested steel 55Cr3 can be considered as a competitive procedure between strain hardening and dynamic softening. The strain hardening mechanism is identified as crystal lattice distortion caused by the generation and multiplication of dislocations, resulting in higher stress for continuous deformation [44,45]. Conversely, the dynamic softening mechanism is a result of rapid atomic diffusion and dislocation annihilation resulting from temperature rise or the stored energy rapid accumulation with the strain rate increasing [45,46].

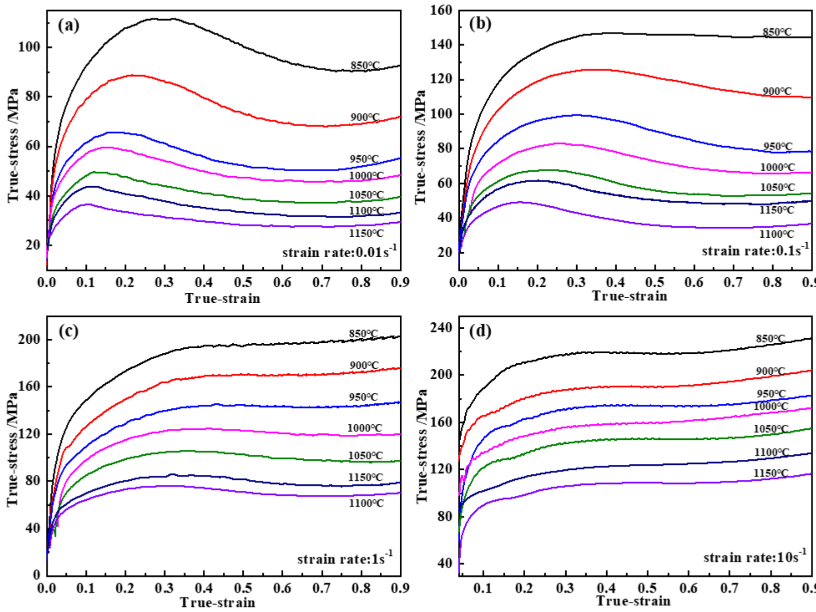

Figure 2. Flow characteristic curves of 55Cr3 steel determined at strain rates of 0.01 s^{-1} (**a**), 0.1 s^{-1} (**b**), 1 s^{-1} (**c**), and 10 s^{-1} (**d**).

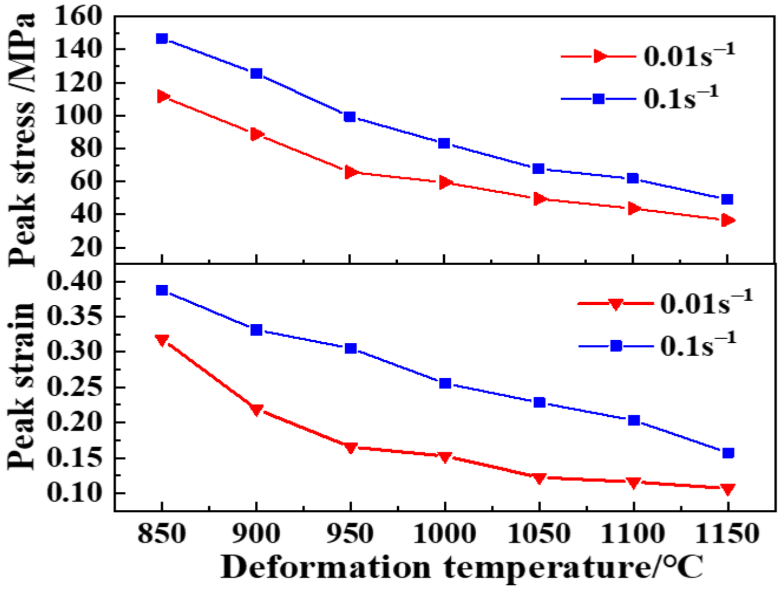

Figure 3. Variation of peak stress and corresponding strain with compressive temperature and strain rate.

3.2. Constitutive Equation

Generally, a constitutive equation can be employed to optimize the hot compression process of metal materials for the reflection of the elevated temperature deformation progress [47]. Among all constitutive models, the Arrhenius constitutive equation could be convenient to describe the correlation among the flow stress (σ), thermal processing temperature (T), and strain rate ($\dot{\varepsilon}$) [48].

$$\dot{\varepsilon} = Kf(\sigma) \cdot exp(-Q/RT) \tag{1}$$

In light of the stress level, the Arrhenius constitutive model can be described as the following three specific expressions:

$$\dot{\varepsilon} = K[\sinh(k\sigma)]^n \cdot exp(-Q/RT)\,) \qquad \text{for all stress levels} \tag{2}$$

$$\dot{\varepsilon} = K_1\sigma^m \cdot exp(-Q/RT)\,) \qquad (k\sigma < 0.8) \tag{3}$$

$$\dot{\varepsilon} = K_2 exp(k'\sigma) \cdot exp(-Q/RT)\,) \qquad (k\sigma > 1.2) \tag{4}$$

Here, $\dot{\varepsilon}$ refers to the strain rate, and σ refers to the flow stress; R corresponds to the universal gas constant with a value of 8.3145 J/(mol·K); T is the absolute temperature with a unit of K; Q is the deformation activation energy in (kJ/mol); K,K_1,$K_2{}'$,m,k', k, n are temperature-independent material constants, $k \approx k'/m$.

Taking the natural logarithm on each side of the formulas, expressions 2 to 4 would be represented as follows:

$$\dot{\varepsilon} = lnK + ln[\sinh(k\sigma)] - (Q/RT) \tag{5}$$

$$\dot{\varepsilon} = lnK_1 + mln(\sigma) - (Q/RT) \tag{6}$$

$$\dot{\varepsilon} = lnK_2 + k'\sigma - (Q/RT) \tag{7}$$

The mean values of m and k' would be obtained using the slopes of the characteristic lines in the $ln\dot{\varepsilon}-ln\sigma_P$ plot and $ln\dot{\varepsilon}-\sigma_P$ plot, which are 7.30125 and 0.07061 MPa^{-1}, respectively (as seen in Figure 4a,b), where $\boldsymbol{\sigma_P}$ refers to the peak stress. Then, the value of k can be acquired from $k \approx k'/m$ = 0.00967 MPa^{-1}.

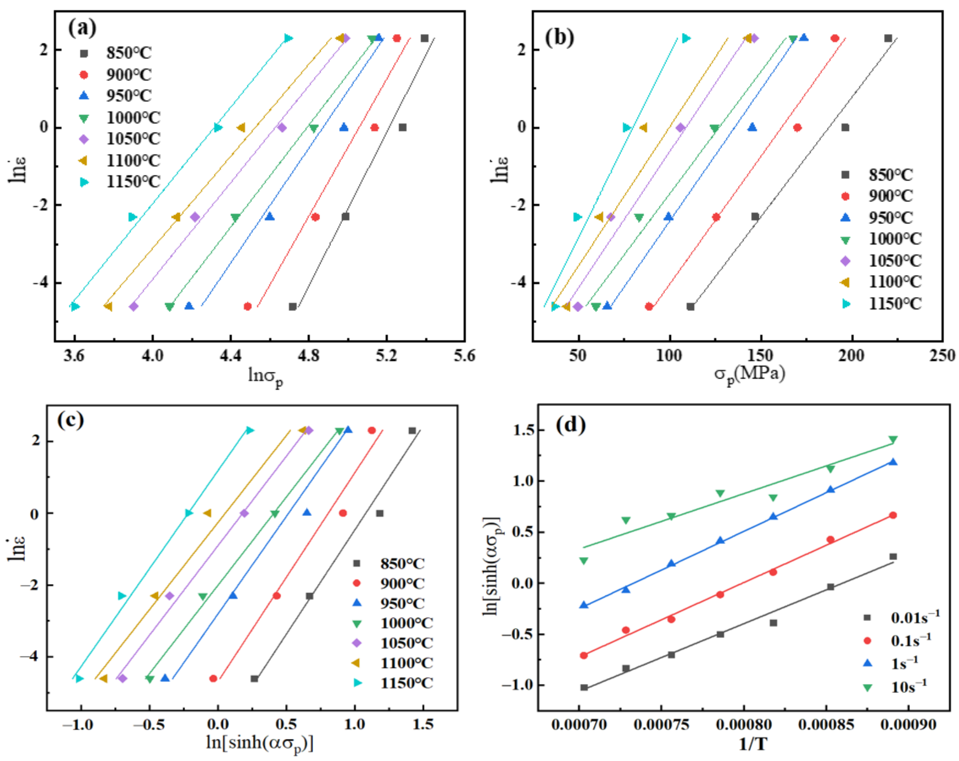

Figure 4. Relationship plot among peak stress, strain rate, and thermal processing temperature of 55Cr3 steel. (**a**) $ln\dot{\varepsilon}$ –$ln\sigma p$; (**b**) $ln\dot{\varepsilon}$ –σp; (**c**) $ln\dot{\varepsilon}$ –$ln[sinh(k\sigma p)]$; (**d**) $ln[sinh(k\sigma p)]$–$1/T$.

According to above calculated parameter k and Equation (5), the n value would be determined according to the average slope of the $ln\dot{\varepsilon}$ $-ln[\sinh(k\sigma_P)]$ plots at given experimental conditions (as illustrated in Figure 4c), whose value is 5.31795. To a particular strain rate, the differentiation of Equation (5) gives

$$Q = Rn\frac{d\{ln[\sinh(k\sigma)]\}}{d(1/T)} = RnK' \tag{8}$$

The average value of K' would be acquired according to the slope of the line in the $ln[\sinh(k\sigma_P)]-1/T$ plot, which is 6728.78514 (as shown in Figure 4d). Thereby, the average thermal activation energy Q at given strain rates can be determined to be 297.503 KJ/mol.

Meanwhile, the Zener–Holloman parameter (Z) with an exponential equation can be applied to describe the effect of thermal processing temperature (T) and strain rate ($\dot{\varepsilon}$) on flow characteristics [49]. This is mathematically represented as the following form:

$$Z = \dot{\varepsilon} \cdot \exp(Q/RT) \tag{9}$$

Furthermore, the following expression is obtained by combining Equation (2) and (9):

$$Z = \dot{\varepsilon} \cdot \exp(Q/RT) = A[\sinh(k\sigma)]^n \tag{10}$$

Besides this, the following expression can be derived from taking the natural logarithm on each side of the above expression.

$$lnZ = lnK + nln[\sinh(k\sigma)] \tag{11}$$

According to Equation (11), it can be clearly observed that lnZ and $ln[sinh(k\sigma)]$ have a linear relationship. The value of A would be derived from taking the intercept of the linear lnZ–$ln[sinh(k\sigma_p)]$ plots. According to the fitting results in Figure 5, the value of lnK as found to be 26.55974, and thus the value of K was calculated to be K = 3.42569 × 10^{11}.

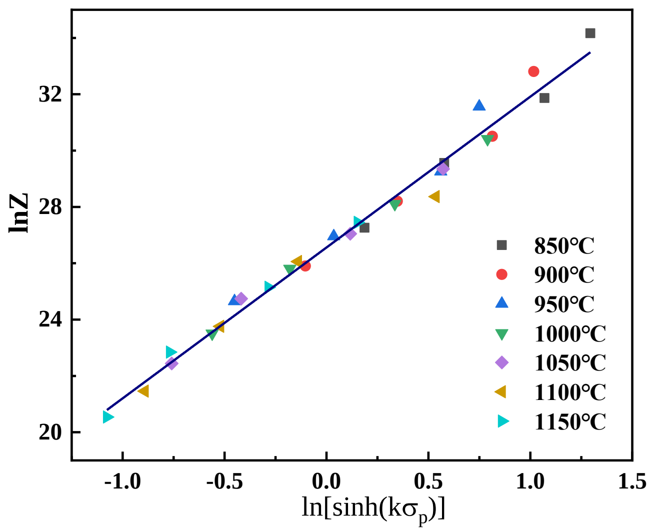

Figure 5. Correlation between lnZ and $ln[sinh(k\sigma_p)]$ for the experimental steel 55Cr3.

Therefore, the flow stress formula (2) can be represented as follows:

$$\dot{\varepsilon} = A[\sinh(k\sigma)]^n \cdot exp(-Q/RT) = 3.425694 \times 10^{11}[sinh(0.009671\sigma)]^{5.31796} \times exp[-297503\ /(RT)] \tag{12}$$

According to Equation (10) and the concept of hyperbolic sine function, the flow stress would be represented as follows:

$$\sigma = \frac{1}{k} ln \left\{ (\frac{Z}{K})^{1/n} + [(\frac{Z}{K})^{2/n} + 1]^{1/2} \right\} \quad (13)$$

According to the above evaluated constants and Equation (13), the constitutive equation of experimental steel connected to the flow stress and the Zener–Holloman parameter would be summarized as follows:

$$\sigma = \frac{1}{0.009671} ln \left\{ (\frac{Z}{3.425694 \times 10^{11}})^{1/5.31795} + [(\frac{Z}{3.425694 \times 10^{11}})^{2/5.31795} + 1]^{1/2} \right\} \quad (14)$$

3.3. Processing Maps

3.3.1. Establishment of a Processing Map

According to the dynamic material model (DMM) summarized by Prasad [50], it is known that the hot working material can be supposed to a power dissipator. In addition, the instantaneous power dissipation (P) is composed of two complementary variables of G component and J co-component.

$$P = \sigma \cdot \dot{\varepsilon} = G + J = \int_0^{\dot{\varepsilon}} \sigma d\dot{\varepsilon} + \int_0^{\sigma} \dot{\varepsilon} d\sigma \quad (15)$$

Here, G refers to the dissipated power in the plastic working process, the majority of which is converted to deformation heat; J is a complementary part of G content for recovery, recrystallization, crack formation, and phase transformation that associates with the metallurgical process; σ and $\dot{\varepsilon}$ are the flow stress and strain rate, respectively.

The power partitioning between G component and J component can be obtained with the strain rate sensitivity index in the following expression [51,52]:

$$m = \frac{dJ}{dG} = \frac{\dot{\varepsilon} d\sigma}{\sigma d\dot{\varepsilon}} = \frac{d(ln\sigma)}{d(ln\dot{\varepsilon})} \quad (16)$$

At the specified strain rate and thermal processing temperature, the expression of flow stress is as follows:

$$\sigma = K \cdot \dot{\varepsilon}^m \quad (17)$$

Here, K is the material constant irrelevant to the experimental conditions.

Then, the expression of the power dissipation J is described as

$$J = \sigma\dot{\varepsilon} - \int_0^{\dot{\varepsilon}} K \cdot \dot{\varepsilon}^m d\dot{\varepsilon} = \frac{m}{m+1} \sigma\dot{\varepsilon} \quad (18)$$

Therefore, to an ideal linear dissipater, $J_{max} = J_{(m=1)} = \frac{\sigma\dot{\varepsilon}}{2}$, while the power dissipation capacity can be predicted with the power dissipation efficiency (η) for nonlinear processes.

$$\eta = \frac{J}{J_{max}} = \frac{2m}{m+1} \quad (19)$$

Thus, power dissipation maps are contour maps at various strain conditions that represent the 3D variation of η with strain rates and thermal processing temperatures.

The flow instabilities must be taken into account, due to the fact that a higher power dissipation factor does not necessarily correspond to a favorable processability.

According to the instability criterion proposed by Prasad and Seshacharyulu for identifying flow instability regimes during the deformation [53], the flow instability related to microstructure will occur in the case of an appearance of ξ (instability parameter) less than zero.

$$\xi(\dot{\varepsilon}) = \frac{\partial\left[ln\left(\frac{m}{m+1}\right)\right]}{\partial(ln\dot{\varepsilon})} + m \leq 0 \tag{20}$$

The instability maps are constituted with instability parameters as a function of strain rate and thermal processing temperature, where the unstable domain is characterized with a negative $\xi(\dot{\varepsilon})$ value. Thus, the processing maps are constructed through superimposing the instability maps over the power dissipation efficiency maps. The former sets the limit to avoid an imperfect microstructure, while the latter reveals the risk area of processing [54]. Therefore, the thermal processing capacity of the metallic materials can be optimized, and the desirable microstructure can be obtained through processing in the high efficiency safety zones and flow stability regions.

3.3.2. Strain Rate Sensitivity Index m

The power dissipation coefficient and instability criterion in the metallic thermal process are dependent on the strain rate sensitivity index of the material. The m-values in different thermal processes are derived according to the fitting cubic polynomic relation between $ln\sigma$ and $ln\dot{\varepsilon}$ at a given strain [55]. The relationship between them can be expressed as follows:

$$ln\sigma = K_0 + K_1 ln\dot{\varepsilon} + K_2(ln\dot{\varepsilon})^2 + K_3(ln\dot{\varepsilon})^3 \tag{21}$$

Here, K_0, K_1, K_2, K_3 are metallic materials constants linked to deformation temperature. Figure 6 presents the variations of the flow stress with strain rates at the true strains of 0.1, 0.3, 0.5, and 0.7, respectively. Thus, the constants K_0, K_1, K_2, K_3 at given thermal processing conditions can be obtained according to the fitting of the relationship between $ln\sigma$ and $ln\dot{\varepsilon}$ at different strains.

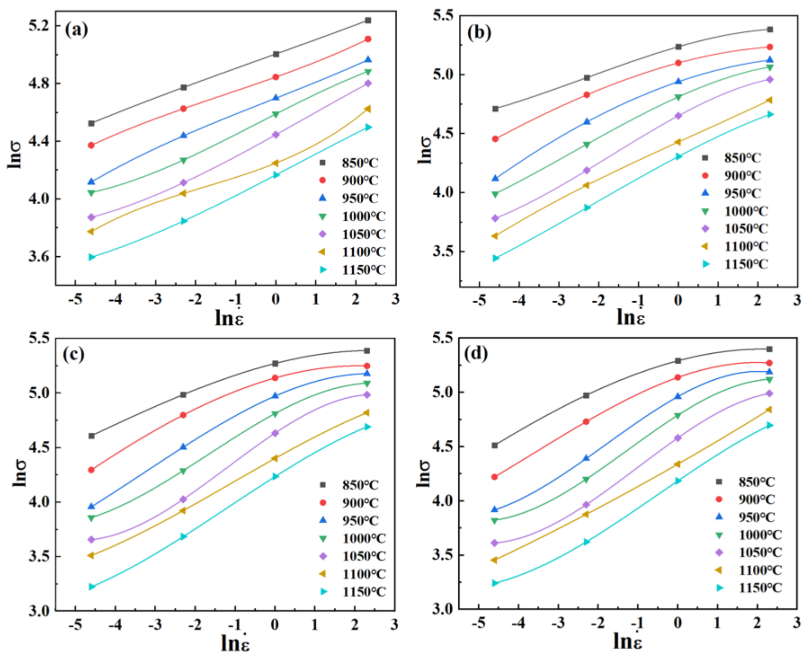

Figure 6. Fitting results to represent the relationship between $ln\sigma$ and $ln\dot{\varepsilon}$ (**a**) $\varepsilon = 0.1$; (**b**) $\varepsilon = 0.3$; (**c**) $\varepsilon = 0.5$; (**d**) $\varepsilon = 0.7$.

Thus, the m-value is the slope of the fitting cubic spline function at given conditions, which can be derived as following expression according to Equations (16) and (21):

$$m = \frac{dJ}{dG} = \frac{d(ln\sigma)}{d(ln\dot{\varepsilon})} = K_1 + 2K_2(ln\dot{\varepsilon}) + 3K_3(ln\dot{\varepsilon})^2 \tag{22}$$

The corresponding m-values at given thermal processing conditions can be easily calculated according to the constants obtained by the above fitting and Equation (22). To discuss the response of the m-value to various thermal–mechanical processes in detail, the smooth 3D surfaces of the m-value were plotted by interpolation, as presented in Figure 7. In general, the m-values vary randomly as a function of the thermal processing temperature, strain, and strain rate. It can be observed from Figure 7 that the maximum m-value increased generally as the strain increased. However, it can be discovered from Figure 7c,d that the negative m-values generally occurred at thermal processes of low thermal processing temperatures and high strain rates. In truth, the domains with a negative m-value were generally regarded as unstable regions. In light of the work of Prasad [54], the negative m-value region generally corresponded to unstable deformation conditions as dynamic strain aging, shear band development, deformation twins, or initiation and propagation of microcracks.

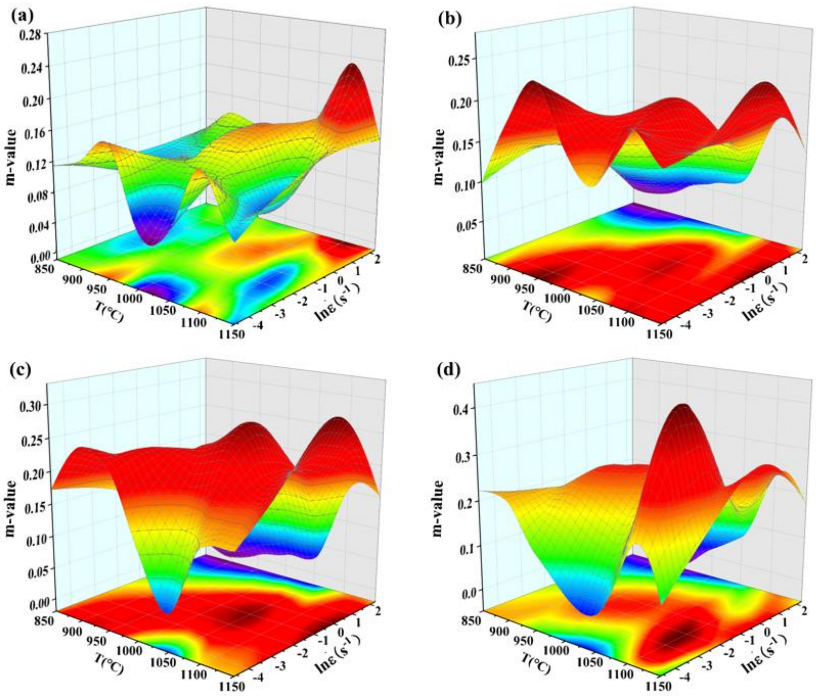

Figure 7. The response of m-values' 3D surfaces at various thermal processing temperatures and strain rates. (**a**) ε = 0.1; (**b**) ε = 0.3; (**c**) ε = 0.5; (**d**) ε = 0.7.

3.3.3. Power Dissipation Efficiency η

The power dissipation efficiency η can be deduced from Equation (19) and the above determined m-values at given thermal processing conditions. Figure 8 demonstrates the contour plot of the power dissipation efficiency at the true strains of 0.1, 0.3, 0.5, and 0.7 that reflect the variation of η as a function of the thermal–mechanical process parameters. The contour number is the value of power dissipation efficiency at the corresponding thermal processing, which describes the proportion of microstructure development throughout the thermal–mechanical process. Overall, as strain increased, so did the power dissipation efficiency. The peak value of η correspondingly increased from 0.35 to 0.54 as the true strain varied from 0.1 to 0.7. However, there were also a few abnormal cases under the deformation conditions of low deformation temperature, large strain, and high strain rate, as demonstrated in Figure 8c,d. Then, the appearance of negative power dissipation efficiency related to the corresponding m-values could be regarded in terms of areas where the metallic flow was instable. Thus, the variation in power dissipation efficiency was ascribed to the general response of m-value to deformation conditions. In addition, the values of η continuously increased as strain rates reduced, while they decreased as deformation temperatures increased, achieving a sequence of peak values at a thermal processing temperature of about 1100 °C and a strain rate of about 0.1 s^{-1}. High power dissipation efficiency is essential in hot working processes, while the region with high η-values does not always correspond to the processing "safe" area, which needs to be further confirmed with the flow unstable criterion.

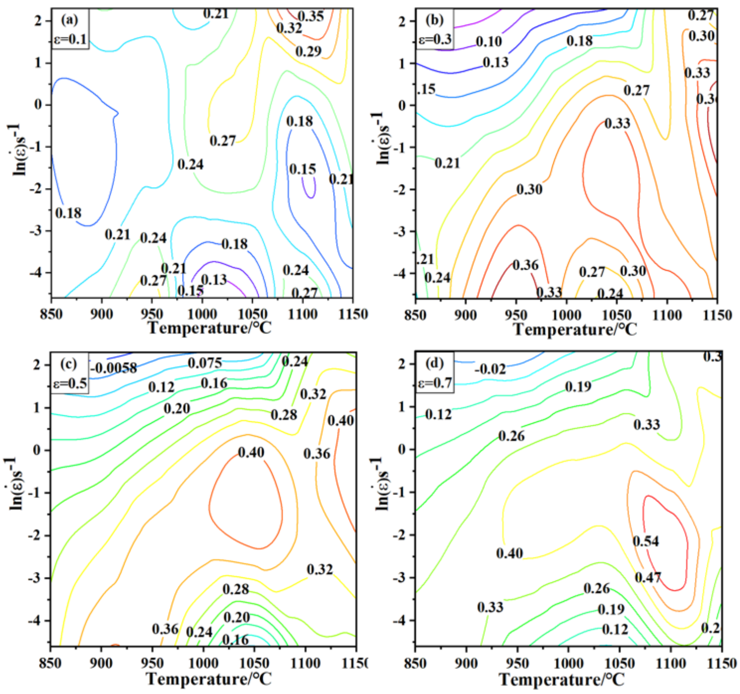

Figure 8. Maps of power dissipation for the experimental steel 55Cr3 at various strains. (**a**) ε = 0.1; (**b**) ε = 0.3; (**c**) ε = 0.5; (**d**) ε = 0.7.

3.3.4. Processing Maps

Variations in the unstable parameters with strain in various thermal–mechanical processes can be determined on the basis of Equation (20) and the above calculated m-values, and then the instability maps can be drawn through the negative instability parameters. Shaded regions represent the instability domains of $\xi(\dot{\varepsilon}) \leq 0$, and others are safe regions. Thus, the processing maps are made through superimposing the corresponding unstable maps on the power dissipation efficiency maps. Figure 9 presents the constructed processing maps for experimental steel 55Cr3 at various true strains, where the contour values correspond to power dissipation constants while the shadows refer to the flow unstable domains. It can be concluded from Figure 9 that the hot working maps were composed of three representative regions, including flow instability regions with negative η and positive $\xi(\dot{\varepsilon})$ as well as positive η and negative $\xi(\dot{\varepsilon})$, and stable domains with positive η and positive $\xi(\dot{\varepsilon})$. Moreover, it is also shown in Figure 9 that these maps represent a similar characteristic, showing an instable region at the low thermal processing temperature as well as high strain rate, which lies in the processing maps' top left corner. Generally, high thermal deformation temperature, low strain rate, and large strain result in a high value of power dissipation efficiency. It can be concluded from Figure 9a that the whole deformation area was a safe domain at the true strain of 0.1. Conversely, the "safe" domains decreased as the strain developed, which revealed that the processing maps were strongly dependent on the strain level, except that the highest η value with the true strain of 0.1 occurred at high thermal processing temperature as well as a high strain rate, and the peak η values at other true strains emerged in high thermal processing temperatures and low strain rates. As a result, the optimum thermal deformation processing windows should be selected from high efficiency regions in a safe processing area. Thus, the applicable hot processing window for experimental steel 55Cr3 is the conditions with thermal processing temperature varying from 1000 to 1150 °C and a strain rate of about 0.1, and with a high η value. It was essential to avoid shaded regions and the areas with negative η values when designing the hot deformation process.

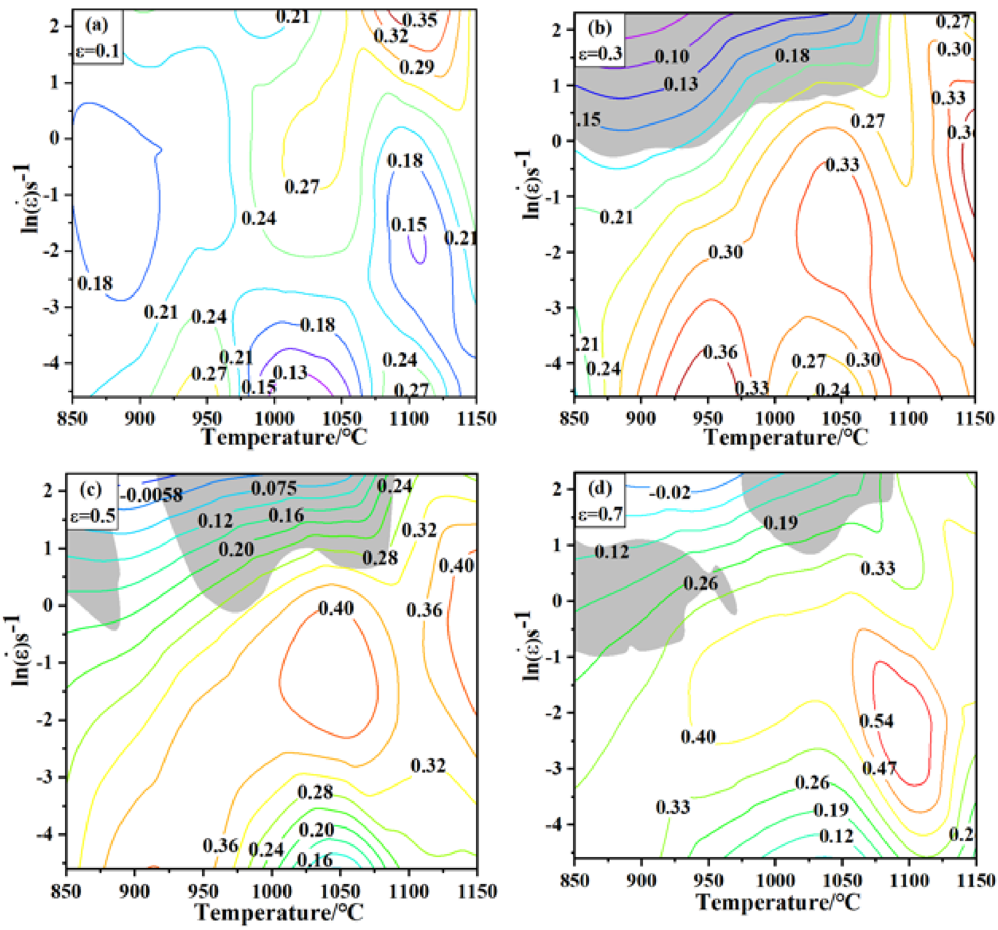

Figure 9. The processing maps of the experimental steel 55Cr3 at various strains. (**a**) ε = 0.1; (**b**) ε = 0.3; (**c**) ε = 0.5; (**d**) ε = 0.7.

4. Conclusions

The influence of thermal–mechanical process parameters on the flow behaviors and thermal processing characteristics in a new designed 55Cr3 spring steel were comprehensively investigated. The main conclusions of this investigation can be summed up as follows:

(1) The flow characteristic of the experimental steel was strongly dictated by deformation parameters such as thermal processing temperature and strain rate. The flow stress and corresponding peak stress increased as the thermal temperature decreased and the strain rate increased. The DRX behavior was attributed to various thermomechanical process parameters, and the low strain rate and high thermal processing temperature facilitated it occurring.

(2) The average thermal activation energy Q at various strain rates was determined to be 297.503 KJ/mol. The Arrhenius constitutive model was developed for the prediction of the metallic flow behaviors. The flow stress expression of the experimental steel 55Cr3

connected to the strain rate and thermal processing temperature were characterized as $\dot{\varepsilon} = 3.425694 \times 10^{11}\ [sinh(0.009671\sigma)]^{5.31796} \times exp[-297503/(RT)]$.

(3) The strain rate sensitivity index, power dissipation coefficient, and instability criterion must be comprehensively considered to identify the stable and instable areas in the processing maps of the experimental steel 55Cr3. The areas where there was one of the negative values among the m-value, η-value, or $\xi(\dot{\varepsilon})$-value should be identified as unstable regions.

(4) The power dissipation coefficient η and instability criterion $\xi(\dot{\varepsilon})$ were found to be dependent on thermomechanical parameters. High deformation temperatures and low strain rates contributed to large power dissipation efficiency. The value of a power dissipation coefficient was approximately proportional to the strain, and the peak η-value rose from 0.35 to 0.54 as the true strain increased from 0.1 to 0.7. The desirable parameters of hot processing for the experimental steel at various strains were that the thermal processing temperature ranged from 1000 to 1150 °C and the strain rate was about 0.1.

Author Contributions: Conceptualization, H.P., J.D. and X.S.; methodology, H.P., Q.F., L.Y. and H.W. (Huiting Wang); validation, H.W. (Hailian Wei), W.L. and H.P.; formal analysis, H.P., Y.F. and S.L.; investigation, H.W. (Hailian Wei), Y.F. and S.L.; data curation, S.L. and H.P.; writing—original draft preparation, H.P., S.L. and Y.F.; writing—review and editing, W.L. and X.S.; visualization, H.P. and H.W. (Huiting Wang); supervision, J.D. and X.S. All authors have read and agreed to the published version of the manuscript.

Funding: This research was funded by the National Natural Science Foundation of China, grant number 51774006, and NSFC-Iron and Steel Joint Fund of the National Natural Science Foundation of China, grant number U1860105; the Natural Science Foundation of Anhui Province, grant number 2008085QE279; and the Key Laboratory of Green Fabrication and Surface Technology of Advanced Metal Materials, grant number GFST2022ZR05.

Institutional Review Board Statement: Not applicable.

Informed Consent Statement: Not applicable.

Data Availability Statement: The data that support the findings of this study are all the own results of the authors.

Conflicts of Interest: The authors declare no conflict of interest.

References

1. Yin, X. Investigation of Non-Metallic Inclusion Plasticization Control for Automotive Suspension Spring Steel. Ph.D. Thesis, University of Science and Technology Beijing, Beijing, China, 2017.
2. Vasu, M.; Hanumanthappa, S.N. Investigation of Cutting Force Tool Tip Temperature and Surface Roughness during Dry Machining of Spring Steel. *Mater. Today Proc.* **2018**, *5*, 7141–7149. [CrossRef]
3. Kumar, T.V.; Chandrasekaran, M.; Padmanabhan, S.; Saravanan, R. Arunkumar. S. Material and design parameters optimization to enhance the life of Anti-Roll bar of commercial truck. *Mater. Today Proc.* **2021**, *37*, 1359–1366. [CrossRef]
4. Nikhil, M.K.; Daspute, D.H. Dynamic analysis of anti-roll bar. *Mater. Today Proc.* **2018**, *5*, 12490–12498. [CrossRef]
5. Mastura, M.T.; Sapuan, S.M.; Mansor, M.R.; Nuraini, A.A. Conceptual design of a natural fibre-reinforced composite automotive anti-roll bar using a hybrid approach. *Int. J. Adv. Manuf. Technol.* **2016**, *91*, 2031–2048. [CrossRef]
6. Muniandy, V.; Mohd Samin, P.; Jamaluddin, H.; Rahman, R.A.; Bakar, S.A.A. Double anti-roll bar hardware-in-loop experiment for active anti-roll control system. *J. Vibroeng.* **2017**, *19*, 2886–2909. [CrossRef]
7. Cronje, P.H.; Els, P.S. Improving off-road vehicle handling using an active anti-roll bar. *J. Terramech.* **2010**, *47*, 179–189. [CrossRef]
8. Kumar, Y.; Siddiqui, R.A.; Upadhyay, Y.; Prajapati, S. Kinematic and Structural Analysis of Independent type suspension system with Anti-Roll bar for Formula Student Vehicle. *Mater. Today Proc.* **2022**, *56*, 2672–2679. [CrossRef]
9. Vu, V.T.; Sename, O.; Dugard, L.; Gaspar, P. H∞/LPV controller design for an active anti-roll bar system of heavy vehicles using parameter dependent weighting functions. *Heliyon* **2019**, *5*, e01827. [CrossRef]
10. Bayrakceken, H.; Tasgetiren, S.; Aslantas, K. Fracture of an automobile anti-roll bar. *Eng. Fail. Anal.* **2006**, *13*, 732–738. [CrossRef]
11. Vu, V.T.; Gaspar, P. Performance and robustness assessment of H∞ active anti-roll bar control system by using a software environment. *IFAC-PapersOnLine* **2019**, *52*, 255–260. [CrossRef]
12. Akiniwa, Y.; Stanzl-Tschegg, S.; Mayer, H.; Wakita, M.; Tanaka, K. Fatigue strength of spring steel under axial and torsional loading in the very high cycle regime. *Int. J. Fatigue* **2008**, *30*, 2057–2063. [CrossRef]

13. Ionut, G.; Dumitru, N.; Rosca, A.; Craciunoiu, N.; Racila, L.; Copilusi, C. Computation of a torsion spring stabilizer bar rigidity and fatigue resistance. *IOP Conf. Ser. Mater. Sci. Eng.* **2019**, *28*, 568–573. [CrossRef]
14. Mastura, M.T.; Sapuan, S.M.; Mansor, M.R.; Nuraini, A.A. Materials selection of thermoplastic matrices for 'green' natural fibre composites for automotive anti-roll bar with particular emphasis on the environment. *Int. J. Precis. Eng. Manuf. Green Technol.* **2018**, *5*, 111–119. [CrossRef]
15. Mastura, M.T.; Sapuan, S.M.; Mansor, M.R.; Nuraini, A.A. Environmentally conscious hybrid bio-composite material selection for automotive anti-roll bar. *Int. J. Adv. Manuf. Technol.* **2016**, *89*, 2203–2219. [CrossRef]
16. Murat, T.M.; Enginar, H.; Eern, E.; Kuralay, N. Reduction of stress concentration at the corner bends of the anti-roll bar by using parametric optimization. *Math. Comput. Appl.* **2011**, *16*, 148–158. [CrossRef]
17. Hui, Y.; Jian, D.; Changan, N.; Jiahang, D.; Xueguang, C.; Kaihong, K.S.; Xingchuan, X. Hot compression deformation behavior and processing maps of Al–0.5 Mg–0.4 Si–0.1 Cu alloy. *J. Mater. Res. Technol.* **2022**, *19*, 4890–4904. [CrossRef]
18. Zhuangzhuang, Z.; Yuyong, C.; Fantao, K.; Xiaopeng, W. The interrupted hot compression of an as-forged titanium matrix composite: Flow softening behavior and deformation mechanism. *J. Mater. Res. Technol.* **2022**, *20*, 821–832. [CrossRef]
19. Yujing, W.; Liang, Z.; Wenzhou, S.; Li, Y.; Xinmei, Z. Hot working characteristics and dynamic recrystallization of delta-processed superalloy 718. *J. Alloys Compd.* **2009**, *474*, 341–346. [CrossRef]
20. Hongzhi, N.; Yuyong, C.; Shulong, X.; Fantao, K.; Changjiang, Z. High temperature deformation behaviors of Ti-45Al-2Nb-1.5 V-1Mo-Y alloy. *Intermetallics* **2011**, *19*, 1767–1774. [CrossRef]
21. Kumar, G.A.; Ujjwal, P.; Ujjwal, M. Flow stress characteristics and microstructural evolution of cast superalloy 625 during hot deformation. *J. Alloys Compd.* **2020**, *844*, 156200. [CrossRef]
22. Di Schino, A. Analysis of phase transformation in high strength low alloyed steels. *Metalurgija* **2017**, *56*, 349–352.
23. Dongjin, S.; Fan, Z.; Ziyu, H.; Wei, G.; Zulai, L. Constitutive equation and dynamic recovery mechanism of high strength cast Al-Cu-Mn alloy during hot deformation. *Mater. Today Commun.* **2022**, *33*, 104199. [CrossRef]
24. Thomas, A.; El-Wahabi, M.; Cabrera, J.M.; Prado, J.M. High temperature deformation of Inconel 718. *J. Mater. Process. Technol.* **2006**, *177*, 469–472. [CrossRef]
25. Jiaoao, L.; Weihong, Z.; Xin, X.; Leiwen, W.; Xuhui, Z.; Wenru, S. Microstructure evolution and dynamic recrystallisation behaviour in hot deformation of Haynes 214 superalloy. *J. Alloys Compd.* **2022**, *919*, 165755. [CrossRef]
26. Jeffrey, M.V.; van der Willem, M.J.; Lindokuhle, V.N. Determination of Critical Transformation Temperatures for the Optimisation of Spring Steel Heat Treatment Processes. *Metals* **2021**, *11*, 1014. [CrossRef]
27. Deng, L.; Haidong, Z.; Guoai, L.; Xuefeng, T.; Pusong, Y.; Zhao, L.; Xinyun, W.; Junsong, J. Processing map and hot deformation behavior of squeeze cast 6082 aluminum alloy. *Trans. Nonferrous Met. Soc. China* **2022**, *32*, 2150–2163. [CrossRef]
28. Jiao, L.; Miaoquan, L.; Bin, W. The correlation between flow behavior and microstructural evolution of 7050 aluminum alloy. *Mater. Sci. Eng. A* **2011**, *530*, 559–564. [CrossRef]
29. Dahai, L.; Haorui, C.; Liang, Y.; Wenqing, Q.; Zhenghua, G.; Zhilu, W. Study on the dynamic recrystallization mechanisms of GH5188 superalloy during hot compression deformation. *J. Alloys Compd.* **2022**, *895*, 162565. [CrossRef]
30. Yongquan, N.; Tao, W.; Fu, M.W.; Li, M.Z.; Linfeng, W.; Zhao, C.D. Competition between work-hardening effect and dynamic-softening behavior for processing as-cast GH4720Li superalloys with original dendrite microstructure during moderate-speed hot compression. *Mater. Sci. Eng. A* **2015**, *642*, 187–193. [CrossRef]
31. Ma, X.; Weidong, Z.; Bin, X.; Yu, S.; Chen, X.; Yuanfei, H. Characterization of the hot deformation behavior of a Ti–22Al–25Nb alloy using processing maps based on the Murty criterion. *Intermetallics* **2012**, *20*, 1–7. [CrossRef]
32. McQueen, H.J.; Evangelista, E. Forging Hot and Cold: Development through the Ages. In *Characterization of Minerals, Metals, and Materials 2014, Proceedings of the a Symposium Sponsored by The Materials Characterization Committee of the Extraction and Processing Division of TMS (The Minerals, Metals & Materials Society): Held during TMS 2014, 143rd Annual Meeting & Exhibition, San Diego Convention Center, San Diego, CA, USA, 16–20 February 2014*; TMS-Minerals, Metals & Materials: San Diego, CA, USA, 2014; pp. 285–296.
33. Yao, L.; Haibo, X.; Jun, W.; Zhou, L.; Fei, L.; Jian, H.; Jingtao, H.; Zhengyi, J. Characteristic flow behaviour prediction and microstructure analysis of a commercial Si–Cr micro-alloyed spring steel under isothermal compression. *Vacuum* **2021**, *186*, 110066. [CrossRef]
34. Yao, L.; Haibo, X.; Jun, W.; Zhou, L.; Fanghui, J.; Hui, W.; Jingtao, H.; Zhengyi, J. Influence of hot compressive parameters on flow behaviour and microstructure evolution in a commercial medium carbon micro-alloyed spring steel. *J. Manuf. Process.* **2020**, *58*, 1171–1181. [CrossRef]
35. Zhigang, W.; Xin, L.; Feiming, X.; Chaobin, L.; Hongwei, L.; Zhang, Q. Dynamic recrystallization behavior and critical strain of 51CrV4 high-strength spring steel during hot deformation. *Jom* **2018**, *70*, 2385–2391. [CrossRef]
36. Hao, W.; Shengping, W.; Hui, H.; Kunyuan, G.; Xiaolan, W.; Wei, W.; Nie, Z.R. Hot deformation behavior and processing map of a new type Al-Zn-Mg-Er-Zr alloy. *J. Alloys Compd.* **2016**, *685*, 869–880. [CrossRef]
37. Ying, W.; Qinglin, P.; Yanfang, S.; Chen, L.; Zhifeng, L. Hot deformation and processing maps of X-750 nickel-based superalloy. *Mater. Des.* **2013**, *51*, 154–160. [CrossRef]
38. Huang, A.; Wang, Z.; Liu, X.; Yuan, Q.; Ye, J.; Zhang, Y. Dynamic strain aging and serrated flow behavior of Cr-Ti-B low carbon steel during warm deformation. *Mater. Charact.* **2021**, *172*, 110828. [CrossRef]

39. Seol, J.B.; Kim, J.G.; Na, S.H.; Park, C.G.; Kim, H.S. Deformation rate controls atomic-scale dynamic strain aging and phase transformation in high-Mn TRIP steels. *Acta Mater.* **2017**, *131*, 187–196. [CrossRef]
40. Jingwei, Z.; Zhengyi, J.; Guoqing, Z.; Wei, D.; Xin, Z.; Laizhu, J. Flow behaviour and constitutive modelling of a ferritic stainless steel at elevated temperatures. *Met. Mater. Int.* **2016**, *22*, 474–487. [CrossRef]
41. Mülders, B.; Zehetbauer, M.; Gottstein, G.; Les, P.; Schafler, E. Large strain work hardening in the alloy Al–1Mg–1Mn at low and intermediate deformation temperatures: Experiments and modelling. *Mater. Sci. Eng. A* **2002**, *324*, 244–250. [CrossRef]
42. Alexandrov, I.V.; Valiev, R.Z. Nanostructures from Severe Plastic Deformation and Mechanisms of Large Strain Work Hardening. *Nanostruct. Mater.* **1999**, *12*, 709–712. [CrossRef]
43. Saad, G.; Fayek, S.A.; Fawzy, A.; Soliman, H.N.; Nassr, E. Serrated flow and work hardening characteristic of Al-5356 alloy. *J. Alloys Compd.* **2010**, *502*, 139–146. [CrossRef]
44. Roy, S.; Mordehai, D. Annihilation of edge dislocation loops via climb during nanoindentation. *Acta Mater.* **2017**, *127*, 351–358. [CrossRef]
45. Arsenlis, A.; Cai, W.; Tang, M.; Rhee, M.; Oppelstrup, T.; Hommes, G.; Pierce, T.G.; Bulatov, V.V. Enabling strain hardening simulations with dislocation dynamics. *Model. Simul. Mater. Sci. Eng.* **2017**, *15*, 553–595. [CrossRef]
46. Li, H.; Xu, M.; Li, Z.; Jiang, R.; Jiang, H.; Li, L.; Mi, Z. Hot deformation behaviour and processing map of a typical Fe-Mn-Si-Cr steel for automotive body structures. *Ironmak. Steelmak.* **2018**, *45*, 937–943. [CrossRef]
47. Yongcheng, L.; Mingsong, C.; Jue, Z. Constitutive modeling for elevated temperature flow behavior of 42CrMo steel. *Comput. Mater. Sci.* **2008**, *42*, 470–477. [CrossRef]
48. Yanhong, X.; Guo, C. Constitutive modelling for high temperature behavior of 1Cr12Ni3Mo2VNbN martensitic steel. *Mater. Sci. Eng. A* **2011**, *528*, 5081–5087. [CrossRef]
49. Sumantra, M.; Venkataramani, R.; Venkata, S.P.; Srinivasan, V.; Kizhakkemadam, V.K. Constitutive equations to predict high temperature flow stress in a Ti-modified austenitic stainless steel. *Mater. Sci. Eng. A* **2009**, *500*, 114–121. [CrossRef]
50. Prasad, Y.V.R.K.; Gegel, H.L.; Doraivelu, S.M.; Malas, J.C.; Morgan, J.T.; Lark, K.A.; Barker, D.R. Modeling of dynamic material behavior in hot deformation: Forging of Ti-6242. *Metall. Trans. A* **1984**, *15*, 1883–1892. [CrossRef]
51. Gang, W.; Xin, L.; Ge, Y.; Zhengwei, G. Hot deformation characteristics and processing maps of AA7075-H18 alloy sheet under hot forming process conditions. *Mater. Lett.* **2022**, *321*, 132413. [CrossRef]
52. Huizhong, L.; Haijun, W.; Zhou, L.; Ming, L.C.; Hongting, L. Flow behavior and processing map of as-cast Mg–10Gd–4.8 Y–2Zn–0.6 Zr alloy. *Mater. Sci. Eng. A* **2010**, *528*, 154–160. [CrossRef]
53. Zhiying, C.; Philip, N. Hot Deformation Behavior and Processing Maps for a Large Marine Crankshaft S34MnV Steel. *Steel Res. Int.* **2018**, *89*, 1700321. [CrossRef]
54. Prasad, Y.V.R.K. Processing maps: A status report. *J. Mater. Eng. Perform.* **2003**, *12*, 638–645. [CrossRef]
55. Huizhong, L.; Haijun, W.; Xiaopeng, L.; Hongting, L.; Ying, L.; Xinming, Z. Hot deformation and processing map of 2519A aluminum alloy. *Mater. Sci. Eng. A* **2011**, *528*, 1548–1552. [CrossRef]